Structural Transitions and Energy Landscape for Cowpea Chlorotic Mottle Virus Capsid Mechanics from Nanomanipulation in Vitro and in Silico

Olga Kononova,[†‡] Joost Snijder,[§] Melanie Brasch,[¶] Jeroen Cornelissen,[¶] Ruxandra I. Dima,[||] Kenneth A. Marx,[†] Gijs J. L. Wuite,[§] Wouter H. Roos,[§*] and Valeri Barsegov[†‡*]

[†]Department of Chemistry, University of Massachusetts, Lowell, Massachusetts; [‡]Moscow Institute of Physics and Technology, Moscow, Russia; [§]Natuur- en Sterrenkunde and LaserLab, Vrije Universiteit, Amsterdam, The Netherlands; [¶]Biomoleculaire Nanotechnologie, Universiteit Twente, Enschede, The Netherlands; and [||]Department of Chemistry, University of Cincinnati, Cincinnati, Ohio

ABSTRACT Physical properties of capsids of plant and animal viruses are important factors in capsid self-assembly, survival of viruses in the extracellular environment, and their cell infectivity. Combined AFM experiments and computational modeling on subsecond timescales of the indentation nanomechanics of Cowpea Chlorotic Mottle Virus capsid show that the capsid's physical properties are dynamic and local characteristics of the structure, which change with the depth of indentation and depend on the magnitude and geometry of mechanical input. Under large deformations, the Cowpea Chlorotic Mottle Virus capsid transitions to the collapsed state without substantial local structural alterations. The enthalpy change in this deformation state ΔH_{ind} = 11.5–12.8 MJ/mol is mostly due to large-amplitude out-of-plane excitations, which contribute to the capsid bending; the entropy change $T\Delta S_{ind}$ = 5.1–5.8 MJ/mol is due to coherent in-plane rearrangements of protein chains, which mediate the capsid stiffening. Direct coupling of these modes defines the extent of (ir)reversibility of capsid indentation dynamics correlated with its (in)elastic mechanical response to the compressive force. This emerging picture illuminates how unique physico-chemical properties of protein nanoshells help define their structure and morphology, and determine their viruses' biological function.

INTRODUCTION

Hierarchical supramolecular systems that spontaneously assemble, disassemble, and self-repair play fundamental roles in biology. Understanding the microscopic structural origin of the physico-chemical properties of these biological assemblies and the mechanisms of their response to controlled mechanical inputs, remains a key research challenge. Single-molecule techniques, such as AFM, have become available to explore physical properties of biological assemblies (1,2). AFM deformation experiments yield information on the particle spring constant, reversibility of deformation, and forces required to distort capsid structures. These techniques triggered significant research effort to characterize the physical and materials properties of a variety of protein shells of plant and animal viruses, and bacteriophages (3). A variety of viruses have been tested including the bacteriophages Φ29, λ, and *HK*97 (4–6), the human viruses Human Immunodeficiency Virus, Noro Virus, Hepatitis B Virus, Adeno Virus, and Herpes Simplex Virus (7–13) and other eukaryotic cell-infecting viruses like Minute Virus of Mice, Triatoma Virus, and Cowpea Chlorotic Mottle Virus (14–16). Yet, due to the high complexity of viruses (~10^4–10^5 amino-acid residues), experimental results are difficult to interpret without input from theoretical modeling. For biotechnological applications, it is essential to have full design control over structure-based physical properties of virus shells, but in most instances a detailed knowledge of these properties is lacking.

Viral capsids possess modular architectures, but strong capsomer intermolecular couplings modulate their properties. Consequently, the properties of the whole system (capsid) might not be given by the sum of the properties of its structural units (capsomers) (17–20). Under these circumstances, one cannot reconstruct the mechanical characteristics of the whole system using only information about the physical properties of its components. Biomolecular simulations have become indispensable for the theoretical exploration of the important dynamical properties and states of biological assemblies (21–23). Yet, the large temporal bandwidth (milliseconds to seconds) required limits the current theoretical capabilities. Theoretical studies employing triangulation of spherical surfaces and bead-spring models of stretching and bending have been used to probe the mechanical deformation and to test the mechanical limits of virus shells (24,25). Questions remain concerning structural details and dynamical aspects of these properties: How do discrete microscopic transitions give rise to the continuous mechanical response of the capsid at the macroscopic level? What are the structural rearrangements that govern the capsid's transition from the elastic to plastic regime of the mechanical deformation?

Here we use a computational approach, which is based upon the notion that the unique features associated with native topology and symmetry of capsomer arrangement, rather than atomic details, govern the physico-chemical properties of virus capsids. Our approach employs a topology-based self-organized polymer (SOP) model (26,27), which provides an accurate description of the polypeptide

Submitted June 29, 2013, and accepted for publication August 26, 2013.

*Correspondence: wroos@few.vu.nl or valeri_barsegov@uml.edu

Editor: Matthias Rief.

0006-3495/13/10/1893/11 $2.00

http://dx.doi.org/10.1016/j.bpj.2013.08.032

chain (28–30), and high-performance computing accelerated on graphics processing units (GPUs) (31,32). By combining AFM-based force measurements with accurate biomolecular simulations we obtain an in-depth understanding of the structural transitions and mechanisms of the mechanical deformation and the transition to the collapsed state in virus shells. By following long (0.01–0.1 s) dynamics of a virus particle, here, for the first time to our knowledge, we directly compare the results of experiments and simulations obtained under similar conditions of force application for the Cowpea Chlorotic Mottle Virus (CCMV) used as a model system (15,33–38).

CCMV is a member of the *Bromoviridae*, a family of single-stranded RNA plant viruses that infect a range of hosts and are the cause of some major crop epidemics (39). The capsid of CCMV is an icosahedral protein shell (triangulation number $T = 3$) with an outer radius $R = 13.2$ nm and average shell thickness of 2.8 nm (3,40) consisting of 180 copies of a single 190 amino-acid-long protein. The shell comprises 60 trimer structural units and exhibits pentameric symmetry at the 12 vertices (pentamer capsomeres) and hexameric symmetry at the 20 faces (hexamer capsomeres) of the icosahedron (Fig. 1). The very good agreement we demonstrated between experiments and simulations allowed us to link the structural transitions in the CCMV capsid with its mechanical properties. The insights into the dynamics of forced compression of this specific viral capsid provide a conceptual framework for describing other virus particles.

MATERIALS AND METHODS

Protein preparation

Purified capsid preparations of empty CCMV particles were obtained using the purification procedures described in Comellas-Aragonès et al. (41). Briefly, the procedure consists of isolation of CCMV particles from cowpea plants 13 days after infection (42,43). After UV/Vis spectroscopy characterization, fast protein liquid chromatography, and running a sample on sodium dodecyl-sulfate polyacrylamide gel electrophoresis to determine the size of the monomers, the virions were examined by transmission electron microscopy. These measurements revealed that the CCMV particles had the expected size of ~28 nm in diameter. The buffer conditions for the imaging and nanoindentation experiments were 50 mM sodium acetate and 1 M sodium chloride (pH = 5.0).

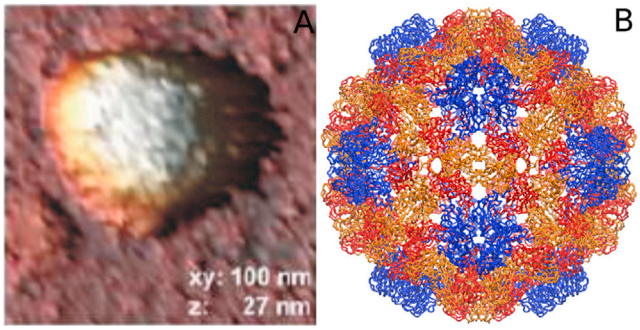

FIGURE 1 The CCMV capsid. (*A*) AFM image of a CCMV capsid ($z_{max} = 30$ nm, scale bar = 20 nm). (*B*) Structure of CCMV (PDB:1CWP): (*blue*) protein domains forming pentamers; (*red* and *orange*) the same protein domains in hexamers. To see this figure in color, go online.

Atomic force microscopy

Hydrophobic glass slides were treated with an alkylsilane (4). The viral samples were kept under liquid conditions at all times; all the experiments were performed at room temperature. Capsid solutions were incubated for ~30 min on the hydrophobic glass slides before the indentation experiments. Model No. OMCL-RC800PSA rectangular, silicon nitride cantilevers (nominal tip radius < 20 nm and spring constant = 0.05 N/m; Olympus, Melville, NY) were calibrated in air, yielding a spring constant of $\kappa = 0.0524 \pm 0.002$ N/m. Viral imaging (44,45) and nanoindentation (3) were performed on a Cervantes AFM (Nanotec, Tres Cantos, Spain). Experimental nanoindentation measurements were carried out using the cantilever velocities $v_f = 0.6$ and 6.0 μm/s. Additional measurements were performed at $v_f = 6.0 \times 10^{-2}$ and 6.0×10^{-3} μm/s. The indentation data were analyzed using a home-written LABVIEW program (National Instruments, Austin, TX), as described previously in Snijder et al. (38).

Self-organized polymer model

In the topology-based self-organized polymer (SOP) model, each residue is described by a single interaction center (C_α-atom). The potential energy function of the protein conformation U_{SOP} specified in terms of the coordinates $\{\mathbf{r}_i\} = \mathbf{r}_1, \mathbf{r}_2, \ldots, \mathbf{r}_N$ (N is the total number of residues) is given by $U_{SOP} = U_{FENE} + U_{NB}^{ATT} + U_{NB}^{REP}$. The finite extensible nonlinear elastic potential $U_{FENE} = -(kR_0^2/2)\sum_{i=1}^{N-1}\log[(1-(r_{i,i+1}-r_{i,i+1}^0)^2)/R_0^2]$ with the spring constant $k = 14$ N/m and the tolerance in the change of a covalent bond distance $R_0 = 2$ Å describes the backbone chain connectivity. The distance between residues i and $i+1$ is $r_{i,i+1}$, and $r^0_{i,i+1}$ is its value in the native structure. We used the Lennard-Jones potential $U_{NB}^{ATT} = \sum_{i,j=i+3}\varepsilon_n[(r_{ij}^0/r_{ij})^{12} - 2(r_{ij}^0/r_{ij})^6]\Delta_{ij}$ to account for the noncovalent interactions that stabilize the native folded state. Here, the summation is performed over all the native contacts in the Protein Data Bank (PDB) structure; we assumed that if the noncovalently linked residues i and j ($|i-j| > 2$) are within the cutoff distance $R_C = 8$ Å in the native state, then $\Delta_{ij} = 1$, and is zero otherwise. The value of ε_n quantifies the strength of the nonbonded interactions. We used $\varepsilon_n = \varepsilon_{inter} = 1.29$ kcal/mol and $\varepsilon_n = \varepsilon_{intra} = 1.05$ kcal/mol for the interchain contacts and intrachain contacts (model parameterization is described in the Supporting Material). The nonnative interactions in the potential $U_{NB}^{REP} = \sum_{i,j=i+2}\varepsilon_r(\sigma_r/r_{ij})^6 + \sum_{i,j=i+3}\varepsilon_r(\sigma_r/r_{ij})^6(1-\Delta_{ij})$ were treated as repulsive. Here, the summation is performed over all the nonnative contacts with the distance $> R_C$. A constraint is imposed on the bond angle formed by residues i, $i+1$, and $i+2$ by including the repulsive potential with parameters $\varepsilon_r = 1$ kcal/mol and $\sigma_r = 3.8$ Å, which determine the strength and the range of the repulsion.

Forced indentation simulations

Dynamic force measurements in silico were performed using the SOP model and GPU-accelerated Langevin simulations, as described in the Supporting Material. We used the CCMV virus capsid, empty of RNA molecules (PDB:1CWP) (40), and a spherical tip of radius $R_{tip} = 5$, 10, and 20 nm to compress the capsid along the two-, three-, and five-fold symmetry axis. The tip-capsid interactions were modeled by the repulsive Lennard-Jones potential, $U_{tip}(r_i) = \varepsilon[\sigma/(r_i - R_{tip})]^6$, where r_i are the ith particle coordinates, $\varepsilon = 4.18$ kJ/mol, and $\sigma = 1.0$ Å. We constrained the bottom portion of the CCMV by fixing five C_α-atoms along the perimeter. The tip exerted the time-dependent force $\boldsymbol{f}(t) = f(t)\boldsymbol{n}$ in the direction $\boldsymbol{n}$ perpendicular to the surface of CCMV shell. The force magnitude $f(t) = r_f t$

increased linearly in time t (force-ramp) with the force-loading rate $r_f = \kappa v_f$ (v_f is the cantilever base velocity and κ is the cantilever spring constant). In the simulations of forward indentation, the tip was moving toward the capsid with $v_f = 1.0$ μm/s and $v_f = 25$ μm/s ($\kappa = 0.05$ N/m). In the simulations of force-quenched retraction for $v_f = 1.0$ μm/s, we reversed the direction of tip motion. In simulations, we control the piezo displacement Z (cantilever base), and the cantilever tip position X. The cantilever base (virtual particle) moves with constant velocity (v_f), which ramps up a force $f(t)$ applied to the capsid through the cantilever tip with the force-loading rate r_f. The resisting force (indentation force) F from the capsid, can be calculated using the energy output.

Analysis of simulation output

To measure the degree of structural similarity between a given conformation and a reference state, we used the structure overlap $\xi(t) = (2N(N-1))^{-1} \sum \Theta(|r_{ij}(t) - r_{ij}^0| - \beta r_{ij}^0)$. In $\Theta(x)$, Heaviside step function, $r_{ij}(t)$ and $r_{ij}{}^0$ are the interparticle distances between the ith and jth residues in the transient and native structure, respectively ($\beta = 0.2$ is the tolerance for the distance change). We analyzed the potential energy U_{SOP} and utilized Umbrella Sampling simulations (see the Supporting Material and Buch et al. (46) and Kumar et al. (47)) to estimate the Gibbs energy (ΔG), enthalpy (ΔH), and entropy (ΔS). We used Normal Mode analysis method to characterize the equilibrium vibrations (see the Supporting Material and Hayward and Groot (48)). We calculated the Hessian matrix for centers of mass of amino acid residues (H_{IJ}). The eigenvalues $\{\lambda_I\}$ and eigenvectors $\{R_I\}$ obtained numerically were used to calculate the spectrum of normal frequencies $\omega_I \propto \sqrt{\lambda_I}$ and normal modes $Q_I = \sum R_{IJ} q_I$, where q_I represents center-of-mass positions. In the Essential Dynamics approach (48), implemented in GROMACS (49), collective modes of motion describing the nonequilibrium displacements of amino acids are projected along the direction of global transition X (indentation depth), characterized by the displacements $\Delta \boldsymbol{X}(t) = \boldsymbol{X}(t) - \boldsymbol{X}_0$ from equilibrium $\boldsymbol{X}_0$ (see the Supporting Material). We diagonalized the covariance matrix $\boldsymbol{C}(t) = \Delta \boldsymbol{X}(t)\ \Delta \boldsymbol{X}(t)^T = \boldsymbol{T}\boldsymbol{\Lambda}\boldsymbol{T}^T$ to compute the matrix of eigenvalues $\boldsymbol{\Lambda}$ and the matrix of eigenvectors $\boldsymbol{T}$. These were used to find the projections $\Delta \boldsymbol{X}(t)$ on each eigenvector $\boldsymbol{t}_I$, $P_I(t) = \boldsymbol{t}_I \Delta \boldsymbol{X}(t)$.

RESULTS

AFM indentation experiments

Before nanoindentation, AFM images of the capsid were recorded as depicted in Fig. 1 *A*. Next, nanoindentation measurements were performed on the center of the CCMV capsid particle, and the corresponding force (F)-indentation (Z) curves (FZ curves) were recorded. The FZ curves quantify the mechanical response of the capsid (indentation force F) as a function of the piezo displacement (reaction coordinate Z). The FZ curves (Fig. 2) revealed that mechanical nanoindentation is a complex stochastic process, which might occur in a single step (all-or-none transition with a single force peak) or through multiple steps (several force peaks). To characterize the experimental FZ curves, we focused on the common features—an initial linear indentation behavior followed by a sharp drop in force (Fig. 2). Next, we performed a fit of a straight line to the initial region of each FZ curve to determine the capsid spring constant k_{cap}, which quantifies the elastic compliance of the capsid, using the relationship $1/K = 1/\kappa + 1/k_{cap}$ for the cantilever-plus-capsid setup. Here, K is the slope in the FZ

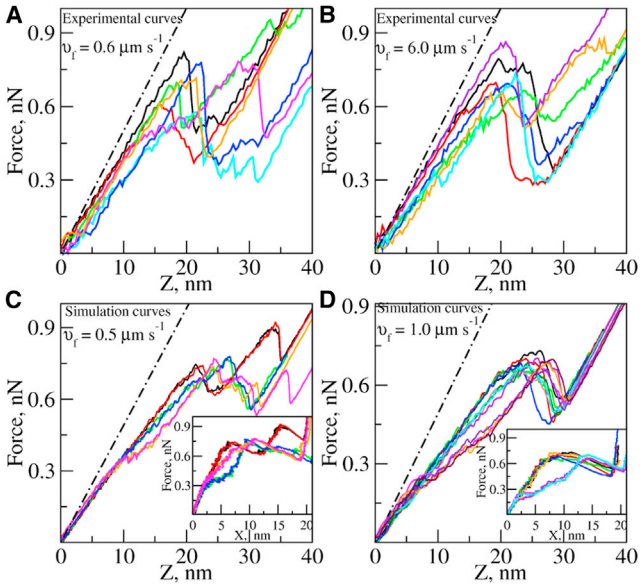

FIGURE 2 Indentation of the CCMV capsid in vitro (*A* and *B*) and in silico along two-, three-, and five-fold symmetry axes (*C* and *D*). Shown in different colors are the most representative trajectories of forced indentation. The force (F)-distance (Z) profiles obtained from experimental AFM measurements for $v_f = 0.6$ and 6.0 μm/s are compared with the theoretical FZ curves obtained for $v_f = 0.5$ and 1.0 μm/s ($R_{tip} = 20$ nm). (*Black dash-dotted control lines*) Cantilever deforming against the glass surface. (*C* and *D, insets*) FX profiles. The values of critical force (F^*, force peaks), transition distance (Z^*), and indentation depth (X^*) are varying. The FZ curves with a single (several) force peak represent single-step (multistep) indentation transitions. To see this figure in color, go online.

curve (Fig. 2), and κ is the cantilever spring constant (see Materials and Methods). We found that the average spring constant of CCMV is $k_{cap} = 0.17$ N/m at a loading rate $v_f = 0.6$ μm/s and $k_{cap} = 0.14$ N/m at $v_f = 6.0$ μm/s (Table 1). Additional experiments showed that k_{cap} does not change much over four decades of v_f (Fig. 3 *A*) (38).

The indentation force, where the linear-like regime in the FZ curve ends, corresponds to the critical force at which the mechanical failure of the capsid occurs. We analyzed the critical forces (F^*) by extracting peak forces observed in the FZ curves, and the corresponding transition distances (Z^*). The average critical force was determined to be $F^* = 0.71$ and 0.72 nN for $v_f = 0.6$ and 6.0 μm/s, respectively, showing that critical force is not much affected by a 10-fold increase in the loading rate in the 0.6–6.0 μm/s-range of v_f used (38). These experiments also showed a good agreement with previously published results (15), where it was found that $k_{cap} \approx 0.15$ N/m and $F^* \approx 0.6$ nN for comparable loading rates (0.02–2 μm/s range). Next, we considered whether mechanical deformation was reversible. We performed measurements for small forward indentation followed by backward movement of the AFM tip, which we refer to as the force-quenched retraction. An example of such measurements clearly shows that there is a considerable difference between the mechanical response of the CCMV particle observed for small and large

TABLE 1 Mechanical properties of the CCMV capsid from indentation measurements in vitro and in silico

Indentation	k_{cap}, N/m	F^*, nN	Z^*, nm
In vitro	0.17 ± 0.01 (0.14 ± 0.02)	0.71 ± 0.08 (0.72 ± 0.07)	21.0 ± 3.6 (20.8 ± 1.7)
In silico	0.11 ± 0.01 (0.11 ± 0.02)	0.77 ± 0.03 (0.71 ± 0.02)	24.7 ± 2.1 (25.5 ± 0.9)

The average values of the spring constant k_{cap}, critical force F^*, and transition distance Z^* calculated by averaging over all FZ curves (all symmetry types). Experimental measurements were performed using $v_f = 0.6$ and 6.0 μm/s; simulations were carried out using $v_f = 0.5$ and 1.0 μm/s (Fig. 2). The experimental results for $v_f = 6.0$ μm/s and simulation results for $v_f = 1.0$ μm/s are shown in parentheses.

deformations (Fig. 3 *B*). Whereas for large piezo displacements ($Z > 35$ nm) the deformation was irreversible with large hysteresis, for small displacements ($Z < 10$ nm) the deformation was completely reversible with almost no hysteresis. These results also agree with our previous findings (15).

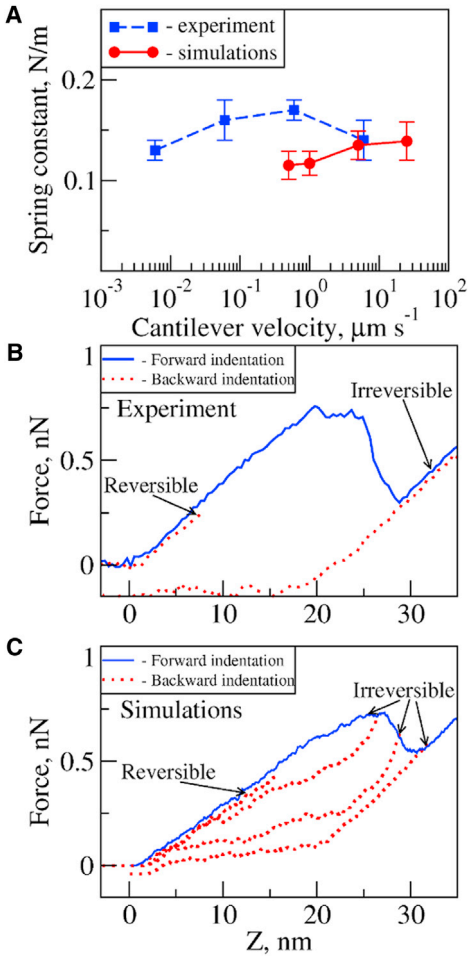

FIGURE 3 (*A*) Log-linear plot of the spring constant of CCMV capsid k_{cap} versus the cantilever velocity v_f. The experimental data (from Snijder et al. (38)) are compared with the results of simulations. (*B* and *C*) Reversible and irreversible deformation of the CCMV capsid obtained experimentally for $v_f = 6.0$ μm/s (*B*), and theoretically for $v_f = 1.0$ μm/s (*C*). Deforming the capsid with a small force of ~0.3 nN (experiment) and ~0.5 nN (simulations) resulted in the reversible mechanical deformation with no hysteresis. Increasing the force beyond ~0.5 nN led to the irreversible deformation: the forward indentation (*solid curves*) and backward retraction (*dotted curves*) do not follow the same path (hysteresis). A slight offset in forward and backward indentation can be seen in the experimental curves, resulting from the directional switching of the piezo. To see this figure in color, go online.

Forced indentation in silico

We performed indentation simulations using a spherical tip of radius $R_{tip} = 20$ nm. The 250-fold computational acceleration on a GPU has enabled us to use experimentally relevant $v_f = 0.5$ and 1.0 μm/s ($\kappa = 0.05$ N/m) and span the experimental 0.1–0.2 s timescale. To compare the results of experiments and simulations, we analyzed the indentation force F as a function of the piezo displacement Z (see Materials and Methods). The theoretical FZ curves (Fig. 2, *C* and *D*) compare well with the experimental FZ profiles (Fig. 2, *A* and *B*). The simulated FZ curves also exhibit single-step transitions and multistep transitions. The latter are more frequently observed under slow force loading when different capsomer-capsomer interactions become sequentially disrupted. We statistically analyzed the spring constant (k_{cap}), and the critical force (F^*) and critical distance (Z^*) for the first disruption step (first force peak), which signifies the mechanical limit of the CCMV shell. The average values of k_{cap}, F^*, and Z^* compare well with their experimental counterparts (Table 1). We also analyzed the dependence of k_{cap} on v_f (including additionally $v_f = 5$ and 25 μm/s) and found that as in experiment, k_{cap} was insensitive to the variation of v_f (Fig. 3 *A*). Next, we performed simulations of force-quenched retraction, where we used the CCMV structures generated in the forward deformation runs for $Z = 15$, 25, 28, and 32 nm as initial conditions. Our simulations (Fig. 3 *C*) agreed with experiments (Fig. 3 *B*) in that indentation is fully reversible for small $Z = 15$-nm displacement but irreversible beyond the critical distance, $Z > 25$ nm.

To summarize, we have obtained an almost quantitative agreement between the results of dynamic force measurements in vitro and in silico. Hence, the SOP model of CCMV provides an accurate description of the capsid mechanical properties, which validates our approach. The good agreement between the results of experiments and simulations allowed us to probe features of the CCMV shell that are not accessible experimentally.

Mechanical properties of CCMV depend on local symmetry

Next, we performed simulations of indentation under slow ($v_f = 1.0$ μm/s) and fast ($v_f = 25$ μm/s) force loading

(R_{tip} = 20 nm). The capsid was indented at different points on its surface: at the symmetry axes of the hexamer capsomeres (three-fold symmetry), the pentamer capsomeres (five-fold symmetry), and at the interface between two hexamers (two-fold symmetry) as described in Fig. S1 in the Supporting Material. Because the FZ curves describe a combined response of the capsid-plus-tip system, they create an impression that the CCMV particle displays a constant elasticity. We found a profile of F versus indentation depth X (FX curve) to be a more sensitive measure of the mechanical properties of the capsid because it reveals fine features of the force spectrum.

The FX curves for the two-fold symmetry axes are displayed in Fig. 4. The FX curves for three- and five-fold symmetry are presented in Fig. S2 and Fig. S3, respectively. We see that the FX profiles are essentially nonlinear curves of varying slope, and that the notion of spring constant should be used with care. Due to thermal fluctuations, mechanical nanoindentation is a stochastic process, which is reflected in that the FX curves show variability even for the same geometry. The mechanical reaction of the capsid is elastic up to $X \approx$ 3–5 nm ($Z \approx$ 8–10 nm; linear regime) and quasi-elastic up to $X \approx$ 8–11 nm ($Z \approx$ 22–25 nm; linear-like regime), regardless of the capsid orientation (Fig. 4 *A*, and see Fig. S2 and Fig. S3). The FX curves generated under fast force loading (v_f = 25 μm/s) showed a slightly steeper slope. Fitting a straight line to the initial portion of FX curves (X < 3 nm) taken at v_f = 1.0 μm/s yielded the spring constant $k_{cap} \approx$ 0.11, 0.10, and 0.12 N/m for two-, three-, and five-fold symmetry, respectively (Table 2).

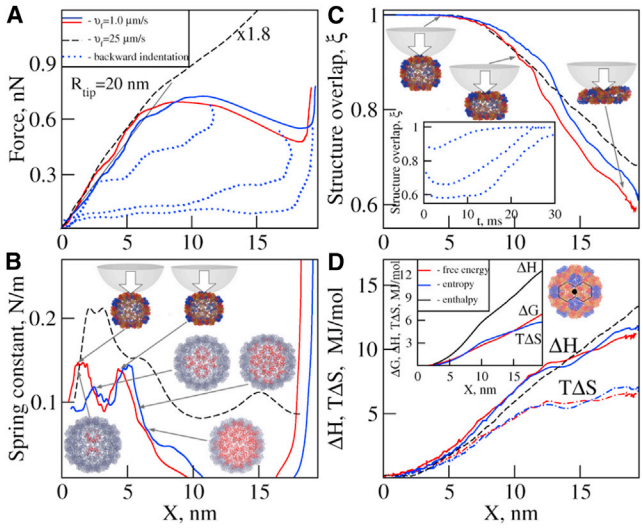

FIGURE 4 Indentation in silico of CCMV capsid along the two-fold symmetry axis (see also Fig. S1). (*Red* and *blue*) The two trajectories. The cantilever tip (R_{tip} = 20 nm) indents the capsid in the direction perpendicular to the capsid surface (v_f = 1.0 μm/s). (*Solid* and *dotted curves*) Results for the forward deformation and backward retraction, respectively; results obtained for v_f = 25 μm/s are shown for comparison (*dashed black curve*). (*A*) The FX curves. (*Gray line*) Linear fit of the curve in the elastic regime (X < 3–5 nm). (*B*) Capsid spring constant, k_{cap} versus X. (*C*) Structure overlap ξ versus X. (*Inset*) Time-dependence of ξ for the backward retraction, which quantifies the progress of capsid restructuring. (*D*) The enthalpy change ΔH and entropy change $T\Delta S$ from the FX curves generated for v_f = 1.0 μm/s (*dashed curve* of ΔH generated for v_f = 25 μm/s is presented for comparison). (*Inset*) Equilibrium energy change ΔG along the reaction coordinate X from Umbrella Sampling calculations. Also shown are the CCMV capsid structures (*top view* and *profile*) for different extents of indentation. (*Red*) Tip-capsid surface contact area (see also Fig. S1). To see this figure in color, go online.

The profile of k_{cap} on X obtained by taking the derivative $k_{cap} = dF/dX$ over the entire range of X turns out to be a sensitive measure of CCMV particle deformation: k_{cap} is significantly varying in the ranges 0.06–0.14, 0.05–0.10, and 0.04–0.12 N/m for the two-, three-, and five-fold symmetry axes, respectively, in the initial deformation regime. Fluctuations in k_{cap} show systematic differences for the icosahedral symmetry axes (Fig. 4, and see Fig. S2 and Fig. S3). When probing along the two- and five-fold axes, the curves of k_{cap} versus X show two maxima: the first maximum is at $X \approx$ 2–3 nm (for two- and five-fold symmetry), and the second maximum is at $X \approx$ 5–6 nm (two-fold symmetry) and 11–12 nm (five-fold symmetry). For the three-fold symmetry, k_{cap} shows one broad skewed peak centered at $X \approx$ 5 nm. Structural analysis revealed that the surface area of the contact between the CCMV shell and the tip changes with the depth of indentation (see Fig. S1). At various stages of deformation, different numbers of protein chains forming capsomers (pentamers and hexamers) cooperate to withstand the mechanical stress.

The collapse transition occurs in the 11–15-nm range (Fig. 4, and see Fig. S2 and Fig. S3). For v_f = 1.0 μm/s, the average critical forces from experiments and simulations agreed (F^* = 0.71 nN; see Fig. 2 and Tables 1 and 2). Here, the bottom portion of the shell becomes increasingly more flat (see *snapshots* in Fig. 4 *C*, and see Fig. S2 and Fig. S3), and the capsid undergoes a spontaneous shape change from a roughly spherical state to a nonspherical collapsed state, which is reflected in the sudden force drop and decrease of k_{cap} to zero (Fig. 4 *B*, and see Fig. S2 and Fig. S3). Under fast loading (v_f = 25 μm/s), force peaks were not detected (Fig. 4 *A*, and see Fig. S2 and Fig. S3). To quantify the extent of the structural collapse, we monitored the structure overlap ξ. In the transition regime, ξ decreased from ξ = 1 (native state) to ξ = 0.65 (collapsed state) for all symmetry types (Fig. 4 *C*, and see Fig. S2 and Fig. S3). Hence, notwithstanding the large-scale transition, the capsid structure remained 65% similar to the native state. For faster v_f = 25 μm/s, ξ decreased by <10%, indicating that fast force loading leaves the local arrangements of capsomers unaffected. At X > 15 nm, CCMV entered the post-collapse, second linear-like regime (Fig. 4, *A* and *B*, and see Fig. S2 and Fig. S3). Here, as the tip approached the solid surface, k_{cap} increased sharply.

Next, we reversed the direction of tip motion using the structures for the collapsed state obtained for Z = 15, 25,

TABLE 2 Mechanical and thermodynamic properties of the CCMV capsid from in silico indentation performed along the two-, three-, and five-fold symmetry axes (see Fig. S1)

Symmetry	F^*, nN	X^*, nm	k_{cap}, N/m	ΔG_{ind}, MJ/mol	ΔH_{ind}, MJ/mol	$T\Delta S_{ind}$, MJ/mol
Two-fold	0.71 ± 0.02	9.1 ± 1.0	0.11 (0.06–0.14)	4.5(6.9)	11.5(12.8)	7.0 (5.8)
Three-fold	0.68 ± 0.02	11.9 ± 0.5	0.10 (0.05–0.10)	5.1(6.8)	11.7(12.6)	6.6(5.8)
Five-fold	0.69 ± 0.02	14.2 ± 0.5	0.12 (0.04–0.12)	4.1(6.5)	12.5(11.5)	8.4(5.1)

Critical force F^*, indentation depth X^*, spring constant k_{cap}, and thermodynamic functions: Gibbs energy change ΔG, enthalpy change ΔH, and entropy change $T\Delta S$. Theoretical estimates were obtained by averaging the results of three trajectories, using $R_{tip} = 20$ nm and $v_f = 1.0$ μm/s (see also Fig. 4, and Fig. S2 and Fig. S3). The values of ΔG_{ind}, ΔH_{ind}, and $T\Delta S_{ind}$ correspond to the total change in these quantities observed at $X = 20$ nm ($Z = 30$ nm) indentation. The range of variation of k_{cap} (from Fig. 4, and see Fig. S2 and Fig. S3) and the equilibrium estimates of ΔG, ΔH, and $T\Delta S$ (from Umbrella Sampling) are shown in parentheses.

28, and 32 nm ($X = 5$, 11, 15, and 19 nm) as initial conditions. In agreement with AFM data (Fig. 3 *B*), the theoretical force-retraction curves for $v_f = 1.0$ μm/s showed that the mechanical compression of CCMV was fully reversible in the elastic regime for $X = 5$ nm (no hysteresis), nearly reversible in the quasi-elastic regime for $X = 11$ nm (small hysteresis), but irreversible after the transition had occurred ($X = 15$ and 19 nm; Fig. 4 *A*, and see Fig. S2 and Fig. S3). We also analyzed the progress of CCMV shell restructuring by monitoring ξ as a function of time (Fig. 4 *C*, and see Fig. S2 and Fig. S3), and found that the CCMV shell recovered its original shape ($\xi = 1$) in the millisecond timescale.

Thermodynamics of CCMV indentation

We evaluated the total work of indentation w by integrating the area under the FX curves. We repeated this procedure for the retraction curves to evaluate the reversible work w_{rev}. Estimation of the relative difference $(w - w_{rev})/w$ showed that in the elastic and quasi-elastic regime ($X < 11$ nm; $Z < 25$ nm) ~12% of w was dissipated. This agrees with the experimental finding that the fraction of energy returned upon retraction is ~90% (15). In the transition range ($11 \text{ nm} \le X \le 15$ nm; $25 \text{ nm} \le Z \le 30$ nm), where the retraction curves showed large hysteresis especially for the three-fold symmetry, $(w - w_{rev})/w \approx 75\%$.

Because $w_{rev} = \Delta G = \Delta H - T\Delta S$, where ΔH and ΔS are the enthalpy change and entropy change, we estimated ΔH and $T\Delta S$. The results for ΔH and $T\Delta S$ for indentation along the two-, three-, and five-fold symmetry axes ($R_{tip} = 20$ nm; $v_f = 1.0$ μm/s) are displayed, respectively, in Fig. 4, and see Fig. S2 and Fig. S3. In the linear regime and linear-like regime ($X < 10$–11 nm), ΔH and $T\Delta S$ display a parabolic dependence on X and $\Delta H \approx T\Delta S$; in the (11–15 nm) transition range and in the post-collapse regime ($X > 15$ nm), ΔH and $T\Delta S$ level off, and $\Delta H > T\Delta S$. The dependence of ΔH on X under fast force loading is more monotonic. The curves of ΔG, ΔH, and $T\Delta S$ attain some constant values ΔG_{ind}, ΔH_{ind}, and $T\Delta S_{ind}$ at $X = 20$ nm, which correspond to the Gibbs energy, enthalpy, and entropy of indentation (Table 2). We also mapped the equilibrium energy landscape ΔG using the Umbrella Sampling simulations (see Materials and Methods) and resolved the profiles of ΔH and $T\Delta S$ (Fig. 4 *D*, *inset*, and see Fig. S2 and Fig. S3). The equilibrium values of ΔG_{ind}, ΔH_{ind}, and $T\Delta S_{ind}$ are accumulated in Table 2. The thermodynamic functions indicate that mechanical compression of the CCMV shell requires a considerable investment of energy, and that ΔG_{ind}, ΔH_{ind}, and $T\Delta S_{ind}$ vary with the local symmetry under the tip.

Mechanical response of CCMV depends on geometry of force application

We performed simulations of the nanoindentation of CCMV along the two-fold symmetry axis using a tip of smaller radius $R_{tip} = 10$ and 5 nm. The FX profiles, spring constant k_{cap}, structure overlap ξ, and thermodynamic functions obtained for $R_{tip} = 10$ nm (see Fig. S4) can be compared with the same quantities obtained for $R_{tip} = 20$ nm (Fig. 4). We present our findings for $R_{tip} = 10$ nm; results for $R_{tip} = 5$ nm show a similar tendency (data not shown). The FX curves for $v_f = 1.0$ (and 25 μm/s) shows a less steep k_{cap}, the collapse transition is less pronounced and starts sooner ($X^* \approx 9$ nm), and the critical force is lower ($F^* \approx 0.6$ nN) for indentation with a smaller tip (see Fig. S4, *A* and *B*). The k_{cap}-versus-X dependence shows two peaks, but the second peak at $X \approx 6$ nm is weaker (compared to the results for $R_{tip} = 20$ nm). The overlap ξ decreased to 0.75, implying that in the collapsed state the CCMV shell remained ≈75% similar to the native state (see Fig. S4 *C*). ΔH and $T\Delta S$ show a familiar parabolic dependence on X (as for $R_{tip} = 20$ nm), but these level off at somewhat lower values (see Fig. S4 *D*). Numerical estimates of k_{cap}, ΔG_{ind}, ΔH_{ind}, and $T\Delta S_{ind}$ obtained for $R_{tip} =$ 10 and 5 nm (Table 3) are directly proportional to the tip size because k_{cap}, ΔG_{ind}, ΔH_{ind}, and ΔS_{ind} all decrease with R_{tip}. We also performed indentation simulations using 10- and 5-nm tips for the three- and five-fold symmetry axes, and arrived at the same conclusions (data not shown).

Equilibrium and nonequilibrium dynamics of CCMV

We calculated the spectra of equilibrium normal modes (see Material and Methods and the Supporting Material) for C_α-atoms for a single hexamer, single pentamer, and

TABLE 3 Mechanical and thermodynamic properties of the CCMV capsid from in silico indentation at $v_f = 1.0$ μm/s, along the two-fold symmetry axis (see Fig. S1)

R_{tip}, nm	k_{cap}, N/m	ΔG_{ind}, MJ/mol	ΔH_{ind}, MJ/mol	$T\Delta S_{ind}$, MJ/mol
20	0.090	4.5	11.5	7.0
10	0.075	3.9	9.6	5.7
5	0.069	1.8	4.9	2.2

Spring constant k_{cap}, and Gibbs energy change ΔG_{ind}, enthalpy change ΔH_{ind}, and entropy change ΔS_{ind} are compared for the spherical tips of different radius $R_{tip} = 20$, 10, and 5 nm. The estimates of k_{cap}, ΔG_{ind}, ΔH_{ind}, and $T\Delta S_{ind}$ are obtained from a single FX curve for each different R_{tip} and correspond to the total change in these quantities observed at $X = 20$ nm (Z = 30 nm) indentation. Simulation data for $R_{tip} = 20$ and 10 nm are shown in Fig. 4 and Fig. S4, respectively.

for the whole CCMV particle (see Fig. S5). Because the spectra for a pentamer and hexamer were identical, we only display the spectrum for a hexamer, which practically overlaps with the spectrum for the CCMV shell, implying that normal displacements of the CCMV shell and its constituents are similar. Analysis of structures revealed that the more global modes of motion in the low-frequency part of the spectrum ($\leq$50 cm^{-1}) involve the out-of-plane expansion-contraction excitations and the in-plane concerted displacements of capsomers. The more local modes (100–250 cm^{-1} range) are small-amplitude displacements of the secondary structure elements. The high-frequency 300–450 cm^{-1} end of the spectrum is dominated by the local vibrations of amino acids (see Fig. S5).

We employed the Essential Dynamics approach (see Materials and Methods and the Supporting Material) to single out the most important types of motion, showing the largest contribution in the direction of global transition (indentation depth X). The far-from-equilibrium essential dynamics modes should not be confused with the equilibrium normal modes. We examined the elastic regime ($X \leq 5$ nm) and the transition regime (11 nm $\leq X \leq$ 15 nm) using the simulation output for the two-fold symmetry (Fig. 4). We resolved the principal coordinates $P_I(t)$, collective variables describing the nonequilibrium dynamics of the system, and analyzed the relative displacement for each Ith mode given by the ratio $\langle (X_I - X_{I0})^2 \rangle / \sum \langle (X_I - X_{I0})^2 \rangle$ of the average squared displacement $\langle (X_I - X_{I0})^2 \rangle$ to the total squared displacement $\sum \langle (X_I - X_{I0})^2 \rangle$. The first two modes account for ~85% of the CCMV dynamics (essential subspace); the remaining modes are negligible in terms of the displacement amplitude.

The CCMV dynamics in the essential subspace is displayed in Fig. 5. In the elastic regime, the first mode (mode 1: 77% of dynamics) corresponds to the large-amplitude out-of-plane compression, which results in the capsid bending. The top and bottom portions of the capsid become flat, whereas the capsid sides expand outward (Fig. 5 *A*). The second mode (mode 2: 8% of dynamics) represents direct coupling of the in-plane displacements of capsomers and the out-of-plane capsid bending, for which the in-plane displacements and the out-of-plane bending occur at the same time. Here we observe that the arrangement of capsomers on the spherical surface change from the more ordered to the less ordered (Fig. 5 *A*). In the transition regime, the in-plane and out-of-plane displacements are coupled. The first mode represents the collapse transition, which is accompanied by the lateral translocation of the capsomers toward the tip-surface contact area (Fig. 5 *B*). The second mode is dominated by the lateral translocation and twisting motions of hexamers and pentamers in the clockwise and counterclockwise direction around their symmetry axes, respectively (Fig. 5 *B*).

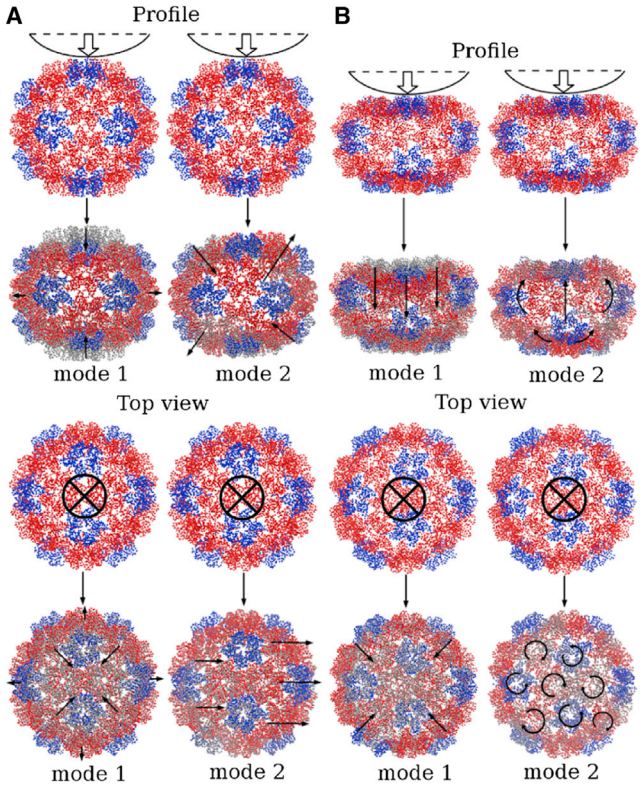

FIGURE 5 Nonequilibrium dynamics of the CCMV shell: shown are the displacement of pentamers (shown in *blue*) and hexamers (shown in *red*) and the structures for the first two modes of the collective excitations (*black arrows*), projected along the reaction coordinate (*large arrow*) in the elastic regime (*A*) and transition regime (*B*). For each mode, the upper structure is the reference state. In the lower structure, we showed the type and amplitude of displacement by juxtaposing the conformation with the reference state (shown in *gray color*). To see this figure in color, go online.

DISCUSSION

By coupling force measurements in vitro and in silico, we have directly compared the experimental data with simulation data for the empty CCMV capsid obtained under

identical conditions of the mechanical force load. Larger variation in the experimental FZ profiles are due to the fact that, in experiments, not only three different icosahedral orientations were probed (two-, three-, and five-fold symmetry) by the AFM tip, but also various intermediate orientations. Smaller drops in the indentation force observed in simulated spectra can be attributed to our overstabilizing the interchain interactions of the CCMV shell and neglecting the hydrodynamic effects. The good overall agreement between experiment and simulations validates our theoretical approach. This has enabled us to interpret the experimental forced indentation patterns in unprecedented detail, with regard to the structural and thermodynamic changes in the CCMV capsid in response to external mechanical deformation.

The main results are:

1. The physical properties of the CCMV shell are dynamic, but local characteristics of the structure, and the mechanical response of the capsid depends not only on the symmetry of the local capsomer arrangement under the tip, but also on the indentation depth.
2. The mechanical characteristics of CCMV—the critical force and transition distance—weakly depend on how rapidly the compressive force is increased.
3. The physical properties of the CCMV particle depend on the geometry of mechanical perturbation, because the mechanical response changes with tip size.
4. The extent to which the mechanical deformation of the CCMV shell can be retraced back reversibly depends on the indentation depth. The dynamic properties, i.e., reversibility and irreversibility of indentation, are correlated with the mechanical characteristics, i.e., elastic response and inelastic deformation.
5. In the elastic regime of deformation, the out-of-plane excitations dominate the near-equilibrium displacements of capsomers, but these and in-plane modes are strongly coupled in the far-from-equilibrium transition range.
6. The entropy change and enthalpy change both contribute to the capsid stiffening, whereas the capsid softening and transition to the collapsed state are driven mainly by the enthalpy change.

Our conclusion about the local nature of physical properties also fits with previous modeling of Hepatitis B Virus, which showed that permanent deformation of the shell was due to local rearrangements of the capsid proteins (21). That the CCMV shell displays multiple modes of mechanical resistance, which depends on the indentation depth, agrees well with recent studies, showing two dynamic regimes to be responsible for the CCMV capsid stiffening and softening (34). The existence of multiple modes is reflected in the nonmonotonic dependence and maxima of k_{cap} as a function of X. The periods of mechanical resistance (stiffening), during which an increasingly larger portion of protein chains find themselves in the tip-shell contact area, are interrupted by the periods when the capsid yields to force (softening). The first peak of k_{cap} at $X \approx 2$–3 nm (Fig. 4 and see Fig. S3) agrees with the previous results from finite element analysis (34). The second peak at $X \approx 6$ nm and $X \approx 11$ nm for the two- and five-fold symmetry described here correspond to the capsid softening beyond $X \approx 10$ nm (34).

The weak dependence of CCMV properties on the rate of change of compressive force is not unexpected, because the positions of transition states and barrier heights on the energy landscape depend upon how force is applied to the system. Under fast force loading ($v_f = 25$ μm/s), the energy pumped into the system is much larger than the energy barrier for the transition to the collapsed state, and this transition is not well-pronounced (no force-drop in the FX curves in Fig. 4, and see Fig. S2 and Fig. S3). The force peaks are observed under slow loading ($v_f = 0.5$–6 μm/s) because the amount of energy is comparable to the energy barrier for the collapse transition. The FZ curves for the CCMV capsid obtained using the finite element analysis (34) agree with our result for $v_f = 25$ μm/s. The FZ profiles from the finite element analysis and our own results also agree in that, under fast force loading, differences in the mechanical response of CCMV for different symmetries disappear.

In single-molecule manipulation on virus particles, mechanical force requires a physical contact between a system and a probe. Hence, their shape, size difference, and the direction of force become important factors. When a virus is indented by a plane ($R_{tip} \gg R$ - radius of a virus shell), all residues in the tip-capsid contact area are pushed in the same direction; when a virus is indented by a small sphere ($R_{tip} \approx R$), different residues are displaced in different directions. Our results show that the mechanical characteristics—FX profile, spring constant, critical force, and indentation depth (see Fig. S4)—all change with probe size, and that ΔG_{ind}, ΔH_{ind}, and $T\Delta S_{ind}$ are directly proportional to R_{tip} (Table 3). A smaller tip means a smaller tip-capsid contact area, and, hence, weaker mechanical response and lower associated energy costs.

In the elastic regime, quasi-elastic regime, and transition regime (Fig. 4, and see Fig. S2 and Fig. S3), the deformation is reversible for short X and almost reversible for longer X. In the post-collapse regime, the mechanical compression is irreversible. These same findings can be rationalized using our Essential Dynamics results (Fig. 5). In the elastic and quasi-elastic regimes, the first mode is dominated by the out-of-plane displacements of pentamers and hexamers. Hence, when a compressive force is quenched, as in the retraction experiments, the first mode provides a mechanism for capsid reshaping, and the amount of energy dissipated is small. In the transition range, the out-of-plane and in-plane displacements are strongly coupled. Here, the capsid is capable of restoring its original shape, but capsid restructuring comes at a cost of exciting additional degrees of freedom and, hence, a larger amount of dissipated energy.

The question exists whether the property of a whole system can be represented by a sum of the properties of its structural elements (50). For the CCMV capsid dynamics at equilibrium, our results from Normal Mode analysis (37,51) provide the affirmative answer. The spectra of eigenmodes for an isolated single pentamer or hexamer and for the whole capsid show only small differences at low frequencies (<50 cm^{-1}), but practically overlap with that for the whole shell in the 50–500 cm^{-1} range (see Fig. S5). The differences in the small-amplitude equilibrium fluctuations of residue positions for local modes are negligible for the penton, hexon, and full capsid. Of course, these modes represent collective motions, which correspond to penton, hexon, and full capsid decompositions; yet, when compared at the whole shell level, these motions in the penton and hexon units, and in the full capsid, are nearly identical (see Fig. S5). Hence, capsomer interactions have little effect on equilibrium properties of CCMV.

Under nonequilibrium conditions of mechanical deformation, the different capsomers play different roles. In this regime, we can no longer use a concept of equilibrium normal modes. We employed the Essential Dynamics approach to characterize large-amplitude displacements of capsomers. Although in the linear regime the main mode of collective motions is dominated by the out-of-plane displacements, there are no pure out-of-plane and in-plane modes either in the elastic regime or in the transition range (Fig. 5). These coupled nonequilibrium essential modes of motion, which accompany the CCMV transition to the collapsed state, cannot be reconstructed using a linear combination of the out-of-plane and the in-plane modes. The concerted in-plane displacements mediate rearrangements of pentamers and hexamers on the CCMV surface, which leads to capsid stiffening reflected in the nonmonotonic dependence of k_{cap} (Fig. 4, and see Fig. S2, Fig. S3, and Fig. S4). These are exact results. Similar findings have been reported by other research groups (52).

We mapped the energy landscape for the mechanical deformation of the CCMV capsid (Fig. 4, and see Fig. S2 and Fig. S3). The similarity of nonequilibrium estimates of ΔG_{ind}, ΔH_{ind}, and ΔS_{ind} (from FX curves) and their equilibrium counterparts (from Umbrella Sampling) implies that slow force loading ($v_f = 1.0$ μm/s) corresponds to near-equilibrium conditions of force application. Both the entropic and enthalpic contributions to ΔG (6.5–6.9 MJ/mol) are important: the entropy change $T\Delta S_{ind}$ (5.1–5.8 MJ/mol) is roughly half the enthalpy change ΔH_{ind} (11.5–12.8 MJ/mol) for all three symmetry types (Table 2). There are variations in the values of ΔG_{ind}, ΔH_{ind}, and $T\Delta S_{ind}$ for different symmetries: these functions for five-fold symmetry differ by ~10% from the same functions for two- and three-fold symmetry (Table 2). Hence, our findings stress the importance of any particular capsid's discrete nature and local protein subunit(s)/capsomer symmetry when virus shells are tested mechanically.

The potential energy of protein chains (U_{SOP}) sharply increases in the transition range where the capsid alters its shape from the convex to the concave (tip-indented convex down). These shape alterations are captured by the enthalpy change ΔH (Fig. 4). Compared to the elastic regime of CCMV deformation ($X < 3$–5 nm), where ΔH increases by ~3 MJ/mol, in the transition region (11 nm $< X <$ 15 nm) ΔH increases threefold to ~10 MJ/mol (Fig. 4 *D*). Here, the large-amplitude out-of-plane displacements mediate the capsid bending inward. Hence, in the quasi-elastic regime before the collapse transition occurs, the out-of-plane collective modes contribute mainly to the enthalpy change ΔH. Although small-amplitude in-plane displacements are coupled to the out-of-plane modes, the main effect from in-plane displacements is concerted transitions—displacements, translocations, and twisting, from the more ordered to the less-ordered phase formed by protein chains (Fig. 5). Hence, the in-plane modes contribute mainly to the entropy change $T\Delta S$, which increases twofold from ~3 MJ/mol in the elastic regime to ~6 MJ/mol in the transition range (Fig. 4). The map of local potential energy for protein chains forming capsomers shows that there is more energy stored in pentamers than in hexamers in the elastic and quasi-elastic regimes (see Fig. S6). This correlates well with the inhomogeneous stress distribution in CCMV capsid found earlier using other methods (53). However, this picture is more mixed in the transition range. Hence, under tension, the same protein chains forming capsomers play different roles in the energy distribution, which change with the indentation depth.

When the capsid is undergoing the global transition to the collapsed state, the average structure of the protein chains forming capsomers is affected, but to a limited extent. This is reflected in the small decrease of the structure overlap to $\xi \approx 0.6$ for the slow force loading ($v_f =$ 1 μm/s). Under fast loading ($v_f = 25$ μm/s), or for smaller tip ($R_{tip} = 10$ nm), the decrease in ξ is even smaller (Fig. 4, and see Fig. S2, Fig. S3, and Fig. S4). This stands in contrast to mechanical protein unfolding where transitioning to the globally unfolded state occurs concomitant with the disruption of native interactions stabilizing the tertiary and secondary structures of the native fold. Hence, in the context of mechanical deformation of a capsid, force-induced spontaneous shape changing does not imply substantial structural transitions on the local scale.

To conclude, we have advanced a conceptual understanding of the physical properties of capsids, have resolved multiple dynamic modes leading to mechanical stiffening and softening effects, have characterized (ir)reversibility of deformation of virions, and have described specific roles of the nonequilibrium collective modes of the capsomers' displacements and their connection to the thermodynamic functions. Because these properties are likely to be shared among different virion classes, the results are significant to an understanding of the nanomechanics of other protein

shells. Biotechnological applications of protein nanocontainers range from catalysis in constrained or altered environments, to transport and delivery of substrates or drugs into cells in nanomedicine, and to providing unique building blocks in nanotechnology architectures (54,55). Our combined in vitro and in silico approach is a strong tool to profile the structural, dynamic, and thermodynamic characteristics of virus capsids and to explore the structure-dynamics relationship for other biologically derived particles.

SUPPORTING MATERIAL

Six figures, one movie, references (56–59), supplemental information and further analysis are available at http://www.biophysj.org/biophysj/supplemental/S0006-3495(13)00979-X.

This work was supported by the Russian Ministry of Education and Science (grant No. 14-A18-21-1239 to V.B.), by the "Physics of the Genome" program grant from Fundamenteel Onderzoek der Materie (to G.J.L.W.), by a NanoNextNL grant (to G.J.L.W.), by a VIDI grant from the Nederlandse Organisatie voor Wetenschappelijk Onderzoek (to W.H.R.), and by the National Science Foundation (grant No. MCB-0845002 to R.I.D.).

REFERENCES

1. Kasas, S., and G. Dietler. 2008. Probing nanomechanical properties from biomolecules to living cells. *Pflugers Arch.* 456:13–27.
2. Engel, A., and D. J. Müller. 2000. Observing single biomolecules at work with the atomic force microscope. *Nat. Struct. Biol.* 7:715–718.
3. Roos, W. H., R. Bruinsma, and G. J. L. Wuite. 2010. Physical virology. *Nat. Phys.* 6:733–743.
4. Ivanovska, I. L., P. J. de Pablo, …, G. J. L. Wuite. 2004. Bacteriophage capsids: tough nanoshells with complex elastic properties. *Proc. Natl. Acad. Sci. USA.* 101:7600–7605.
5. Ivanovska, I. L., G. J. L. Wuite, …, A. Evilevitch. 2007. Internal DNA pressure modifies stability of WT phage. *Proc. Natl. Acad. Sci. USA.* 104:9603–9608.
6. Roos, W. H., I. Gertsman, …, G. J. L. Wuite. 2012. Mechanics of bacteriophage maturation. *Proc. Natl. Acad. Sci. USA.* 109:2342–2347.
7. Kol, N., Y. Shi, …, I. Rousso. 2007. A stiffness switch in human immunodeficiency virus. *Biophys. J.* 92:1777–1783.
8. Baclayon, M., G. K. Shoemaker, …, W. H. Roos. 2011. Prestress strengthens the shell of Norwalk virus nanoparticles. *Nano Lett.* 11:4865–4869.
9. Liashkovich, I., W. Hafezi, …, V. Shahin. 2008. Exceptional mechanical and structural stability of HSV-1 unveiled with fluid atomic force microscopy. *J. Cell Sci.* 121:2287–2292.
10. Pérez-Berná, A. J., A. Ortega-Esteban, …, C. San Martín. 2012. The role of capsid maturation on adenovirus priming for sequential uncoating. *J. Biol. Chem.* 287:31582–31595.
11. Roos, W. H., K. Radtke, …, G. J. L. Wuite. 2009. Scaffold expulsion and genome packaging trigger stabilization of Herpes Simplex Virus capsids. *Proc. Natl. Acad. Sci. USA.* 106:9673–9678.
12. Roos, W. H., M. M. Gibbons, …, G. J. L. Wuite. 2010. Squeezing protein shells: how continuum elastic models, molecular dynamics simulations, and experiments coalesce at the nanoscale. *Biophys. J.* 99:1175–1181.
13. Snijder, J., V. S. Reddy, …, G. J. L. Wuite. 2013. Integrin and defensin modulate the mechanical properties of adenovirus. *J. Virol.* 87:2756–2766.
14. Carrasco, C., A. Carreira, …, P. J. de Pablo. 2006. DNA-mediated anisotropic mechanical reinforcement of a virus. *Proc. Natl. Acad. Sci. USA.* 103:13706–13711.
15. Michel, J. P., I. L. Ivanovska, …, C. F. Schmidt. 2006. Nanoindentation studies of full and empty viral capsids and the effects of capsid protein mutations on elasticity and strength. *Proc. Natl. Acad. Sci. USA.* 103:6184–6189.
16. Snijder, J., C. Uetrecht, …, W. H. Roos. 2013. Probing the biophysical interplay between a viral genome and its capsid. *Nat. Chem.* 5: 502–509.
17. Berendsen, H. J. C., and S. Hayward. 2000. Collective protein dynamics in relation to function. *Curr. Opin. Struct. Biol.* 10:165–169.
18. Bura, E., D. K. Klimov, and V. Barsegov. 2008. Analyzing forced unfolding of protein tandems by ordered variates, 2: dependent unfolding times. *Biophys. J.* 94:2516–2528.
19. Joshi, H., F. Momin, …, R. I. Dima. 2010. Exploring the contribution of collective motions to the dynamics of forced-unfolding in tubulin. *Biophys. J.* 98:657–666.
20. Lange, O. F., and H. Grubmüller. 2008. Full correlation analysis of conformational protein dynamics. *Proteins.* 70:1294–1312.
21. Arkhipov, A., W. H. Roos, …, K. Schulten. 2009. Elucidating the mechanism behind irreversible deformation of viral capsids. *Biophys. J.* 97:2061–2069.
22. Phelps, D. K., B. Speelman, and C. B. Post. 2000. Theoretical studies of viral capsid proteins. *Curr. Opin. Struct. Biol.* 10:170–173.
23. Zink, M., and H. Grubmüller. 2009. Mechanical properties of the icosahedral shell of Southern Bean Mosaic virus: a molecular dynamics study. *Biophys. J.* 96:1350–1363.
24. Vliegenthart, G. A., and G. Gompper. 2006. Mechanical deformation of spherical viruses with icosahedral symmetry. *Biophys. J.* 91:834–841.
25. Buenemann, M., and P. Lenz. 2007. Mechanical limits of viral capsids. *Proc. Natl. Acad. Sci. USA.* 104:9925–9930.
26. Hyeon, C., R. I. Dima, and D. Thirumalai. 2006. Pathways and kinetic barriers in mechanical unfolding and refolding of RNA and proteins. *Structure.* 14:1633–1645.
27. Mickler, M., R. I. Dima, …, M. Rief. 2007. Revealing the bifurcation in the unfolding pathways of GFP by using single-molecule experiments and simulations. *Proc. Natl. Acad. Sci. USA.* 104:20268–20273.
28. Dima, R. I., and H. Joshi. 2008. Probing the origin of tubulin rigidity with molecular simulations. *Proc. Natl. Acad. Sci. USA.* 105:15743–15748.
29. Lin, J. C., and D. Thirumalai. 2008. Relative stability of helices determines the folding landscape of adenine riboswitch aptamers. *J. Am. Chem. Soc.* 130:14080–14081.
30. Zhmurov, A., A. E. X. Brown, …, V. Barsegov. 2011. Mechanism of fibrin(ogen) forced unfolding. *Structure.* 19:1615–1624.
31. Zhmurov, A., R. I. Dima, …, V. Barsegov. 2010. Sop-GPU: accelerating biomolecular simulations in the centisecond timescale using graphics processors. *Proteins.* 78:2984–2999.
32. Zhmurov, A., K. Rybnikov, …, V. Barsegov. 2011. Generation of random numbers on graphics processors: forced indentation in silico of the bacteriophage HK97. *J. Phys. Chem. B.* 115:5278–5288.
33. Cieplak, M., and M. O. Robbins. 2010. Nanoindentation of virus capsids in a molecular model. *J. Chem. Phys.* 132:015101.
34. Gibbons, M. M., and W. S. Klug. 2008. Influence of nonuniform geometry on nanoindentation of viral capsids. *Biophys. J.* 95:3640–3649.
35. Johnson, J. E., and J. A. Speir. 1997. Quasi-equivalent viruses: a paradigm for protein assemblies. *J. Mol. Biol.* 269:665–675.
36. Johnson, J. M., J. Tang, …, A. Zlotnick. 2005. Regulating self-assembly of spherical oligomers. *Nano Lett.* 5:765–770.
37. May, E. R., A. Aggarwal, …, C. L. Brooks, 3rd. 2011. Viral capsid equilibrium dynamics reveals nonuniform elastic properties. *Biophys. J.* 100:L59–L61.

38. Snijder, J., I. L. Ivanovska, …, G. J. L. Wuite. 2012. Probing the impact of loading rate on the mechanical properties of viral nanoparticles. *Micron.* 43:1343–1350.

39. Scott, S. W. 2006. *Bromoviridae* and allies. *In* Encyclopedia of Life Sciences John Wiley, Chichester, UK.

40. Speir, J. A., S. Munshi, …, J. E. Johnson. 1995. Structures of the native and swollen forms of Cowpea Chlorotic Mottle Virus determined by x-ray crystallography and cryo-electron microscopy. *Structure.* 3:63–78.

41. Comellas-Aragonès, M., H. Engelkamp, …, R. J. M. Nolte. 2007. A virus-based single-enzyme nanoreactor. *Nat. Nanotechnol.* 2:635–639.

42. Verduin, B. J. M. 1974. The preparation of CCMV-protein in connection with its association into a spherical particle. *FEBS Lett.* 45:50–54.

43. Verduin, B. J. M. 1978. Degradation of Cowpea Chlorotic Mottle Virus ribonucleic acid in situ. *J. Gen. Virol.* 39:131–147.

44. Baclayon, M., G. J. L. Wuite, and W. H. Roos. 2010. Imaging and manipulation of single viruses by atomic force microscopy. *Soft Matter.* 6:5273–5285.

45. Kuznetsov, Y. G., and A. McPherson. 2011. Atomic force microscopy in imaging of viruses and virus-infected cells. *Microbiol. Mol. Biol. Rev.* 75:268–285.

46. Buch, I., S. Kashif Sadiq, and G. De Fabritiis. 2011. Optimized potential of mean force calculations for standard binding free energies. *J. Chem. Theory Comput.* 7:1765–1772.

47. Kumar, S., J. M. Rosenberg, …, P. A. Kollman. 1992. The weighted histogram analysis method for free-energy calculations on biomolecules. I. The method. *J. Comput. Chem.* 13:1011–1021.

48. Hayward, S., and B. L. de Groot. 2008. Normal modes and essential dynamics. *Methods Mol. Biol.* 443:89–106.

49. Lindahl, E., B. Hess, and D. van der Spoel. 2001. GROMACS 3.0: a package for molecular simulation and trajectory analysis. *J. Mol. Model.* 7:306–317.

50. Zhmurov, A., R. I. Dima, and V. Barsegov. 2010. Order statistics theory of unfolding of multimeric proteins. *Biophys. J.* 99:1959–1968.

51. Tama, F., and C. L. Brooks, 3rd. 2005. Diversity and identity of mechanical properties of icosahedral viral capsids studied with elastic network normal mode analysis. *J. Mol. Biol.* 345:299–314.

52. Yang, L., G. Song, and R. L. Jernigan. 2007. How well can we understand large-scale protein motions using normal modes of elastic network models? *Biophys. J.* 93:920–929.

53. Zandi, R., and D. Reguera. 2005. Mechanical properties of viral capsids. *Phys. Rev. E Stat. Nonlin. Soft Matter Phys.* 72:021917.

54. Fischlechner, M., and E. Donath. 2007. Viruses as building blocks for materials and devices. *Angew. Chem. Int. Ed. Engl.* 46:3184–3193.

55. Ma, Y., R. J. Nolte, and J. J. Cornelissen. 2012. Virus-based nanocarriers for drug delivery. *Adv. Drug Deliv. Rev.* 64:811–825.

56. Ferrara, P., J. Apostolakis, and A. Caflisch. 2002. Evaluation of a fast implicit solvent model for molecular dynamics simulations. *Proteins.* 46:24–33.

57. Amadei, A., A. B. M. Linssen, and H. J. C. Berendsen. 1993. Essential dynamics of proteins. *Proteins.* 17:412–425.

58. Barsegov, V., D. Klimov, and D. Thirumalai. 2006. Mapping the energy landscape of biomolecules using single molecule force correlation spectroscopy (FCS): Theory and applications. *Biophys. J.* 90:3827–3841.

59. Kononova, O., L. Jones, and V. Barsegov. 2013. Order statistics inference for describing topological coupling and mechanical symmetry breaking in multidomain proteins. *J. Chem. Phys.* 139:121913–121925.